

Infrared fixed point of SU(2) gauge theory with six flavors

Viljami Leino,^{1,2,*} Kari Rummukainen,^{1,2,†} Joni Suorsa,^{1,2,‡} Kimmo Tuominen,^{1,2,§} and Sara Tähtinen,^{1,2,¶}

¹*Department of Physics, University of Helsinki*

P.O. Box 64, FI-00014, Helsinki, Finland

²*Helsinki Institute of Physics,*

P.O. Box 64, FI-00014, Helsinki, Finland

We compute the running of the coupling in SU(2) gauge theory with six fermions in the fundamental representation of the gauge group. We find a strong evidence that this theory has an infrared stable fixed point at strong coupling and measure also the anomalous dimension of the fermion mass operator at the fixed point. This theory therefore likely lies close to the boundary of the conformal window and will display novel infrared dynamics if coupled with the electroweak sector of the Standard Model.

I. INTRODUCTION

Determination of the vacuum phase of an SU(N) gauge theory as a function of the number of massless flavors of Dirac fermions, N_f , and their representations presents a challenge for our basic understanding of gauge theory dynamics at strong coupling. A lot of effort in the field of lattice gauge theory has been devoted to address the existence and properties of infrared fixed point (IRFP), which appears when N_f is between a critical lower limit N_f^{crit} and the loss of asymptotic freedom. The bounds depend on N and the fermion representation. For recent reviews see [1–3]. A much studied benchmark case is SU(2) gauge theory with two Dirac fermions in the adjoint representation [4–18], where the results indicate the existence of an IRFP.

In SU(2) gauge theory with fermions in the fundamental representation the precise dependence on N_f remains uncertain, despite a large number of recent studies on the lattice [19–24]. The upper edge of the conformal window is robust: the asymptotic freedom is lost at $N_f = 11$, where the 1-loop β -function coefficient changes sign. Just below the upper edge, at 10 flavors the theory has a perturbatively stable Banks-Zaks type infrared fixed point [25], which has also been observed on the lattice [21]. Recently, simulations of the 8 flavor theory have also shown the existence of a fixed point [24]. On the other hand, the theory with $N_f = 2$ is well below the conformal window and breaks the chiral symmetry according to the expected pattern, and the theory with $N_f = 4$ is expected to fall within this category as well [21]. However, for $N_f = 6$ the previous results remain so far inconclusive [20–23].

In perturbation theory the β -function is known up to

5-loop order in the $\overline{\text{MS}}$ scheme [26]. In SU(2) gauge theory with $N_f = 6$ fundamental representation fermions the β -function has a non-trivial zero (i.e an IRFP) up to 4-loop order. In the 5-loop expansion of the β -function the IRFP vanishes. Similar behavior has been observed in SU(3) with $N_f = 12$ [27]. However, the SU(2) 5-loop β -function shows peculiar behaviour as N_f is varied: it predicts an IRFP in two disconnected domains, at $3.0 \lesssim N_f \lesssim 5.8$ and $8.6 \lesssim N_f < 11$. $N_f = 6$ lies between these ranges. This kind of behaviour is clearly unphysical, and shows that perturbation theory cannot be quantitatively relied upon when the fixed point appears at strong coupling.

In this article we give strong evidence that the six flavor theory indeed has an IRFP at strong coupling. The result is based on a thorough state-of-the-art measurements of the running coupling and the anomalous dimension of the fermion mass operator. We use the HEX smeared Wilson-clover fermion lattice action and measure the coupling using the Yang-Mills gradient flow [28, 29] in conjunction with the finite volume step scaling function with Dirichlet (“Schrödinger functional”) boundary conditions [30]. The value of the coupling at IRFP, g_*^2 , is scheme dependent and hence depends on the gradient flow time. With our benchmark scheme we find $g_*^2 = 14.5(4)_{-1.2}^{+0.4}$ with statistical and systematic errors.

We also measure two scheme independent quantities at the IRFP: the mass anomalous dimension γ_m^* and the leading irrelevant critical exponent γ_g^* , which gives the slope of the β -function at IRFP. The mass anomalous dimension is measured using two different methods: the mass step scaling method [31] and the Dirac operator spectral density method [32]. At the fixed point we observe $\gamma_m^* = 0.283(2)_{-0.01}^{+0.01}$. The slope of the β -function is directly measurable from the step scaling function of the coupling, obtaining $\gamma_g^* = 0.648(97)_{-0.1}^{+0.16}$. In contrast to the value of the fixed point coupling, we observe that γ_g^* remains independent of the gradient flow time, in accord with the scheme independence of this quantity.

This paper is structured as follows: In section II we

* viljami.leino@helsinki.fi

† kari.rummukainen@helsinki.fi

‡ joni.suorsa@helsinki.fi

§ kimmo.i.tuominen@helsinki.fi

¶ sara.tahtinen@helsinki.fi

define the model and outline the simulation methods. The numerical results are presented for running coupling, leading irrelevant exponent, and mass anomalous dimension, in sections III, IV, and V respectively. In section VI we present our conclusions.

II. LATTICE IMPLEMENTATION

The model we use and the algorithmic details we apply are described in detail in [17, 24], and our discussion here will be brief so that we can then focus on the results we obtain in the case of $N_f = 6$. The model is defined by the lattice action

$$S = (1 - c_g)S_G(U) + c_g S_G(V) + S_F(V) + c_{\text{SW}}\delta S_{\text{SW}}(V).$$

The smeared gauge link V is defined by hypercubic truncated stout smearing (HEX smearing) [33], and we mix smeared, $S_G(V)$, and unsmeared, $S_G(U)$, Wilson gauge actions with mixing parameter $c_g = 0.5$. This partial smearing allows us to reach significantly larger couplings by avoiding the unphysical bulk phase transition in the region of interest of the parameter space [34]. We use clover Wilson fermion action with the Sheikholeslami-Wohlert coefficient set to tree level value of unity, $c_{\text{SW}} = 1$, which is the standard choice for smeared clover fermions. We have verified that this value is very close to the true non-perturbatively fixed c_{SW} coefficient, canceling most of the $O(a)$ errors.

On a lattice of size L^4 we use Dirichlet boundary conditions at the temporal boundaries $x_0 = 0, L$ by setting the gauge link matrices $U = V = 1$ and the fermion fields to zero. The spatial boundaries are periodic. These boundary conditions enable simulations at vanishing fermion mass, and allow the mass anomalous dimension to be measured using the same configurations as for the running coupling.

We run our simulations using the hybrid Monte Carlo algorithm with 2nd order Omelyan integrator [35, 36] and chronological initial values for the fermion matrix inversions [37]. We tune the step length to have an acceptance rate larger than 85%. We run the simulations with bare couplings varying within the range

$$\beta_L \equiv 4/g_0^2 \in [0.5, 8] \quad (1)$$

and tune the hopping parameter $\kappa_c(\beta_L)$ so that the absolute value of the PCAC fermion mass [38] is less than 10^{-5} at lattices of size 24^4 . The same critical hopping parameter values are used for all the lattice sizes, and for each β_L (and corresponding $\kappa_c(\beta_L)$). The critical hopping parameters are available in the Table III. We use lattices of size $L = 8, 10, 12, 16, 18, 20, 24$, and 30 chosen to allow step scaling with either $s = 2$ or $s = 3/2$. For our analysis we choose $s = 3/2$ as it includes more pairs within the larger lattices. We generate $(5 - 100) \cdot 10^3$

trajectories for each combination of β_L and L . For the exact number of trajectories used, see Table IV.

To define the running coupling, we apply the Yang-Mills gradient flow method [28–30]. This method defines a flow that smooths the gauge fields and removes UV divergences and automatically renormalizes gauge invariant objects [39]. The method is set up by introducing a fictitious flow time t and studying the evolution of the flow gauge field $B_\mu(x, t)$ according to the flow equation

$$\partial_t B_\mu = D_\nu G_{\nu\mu}, \quad (2)$$

where $G_{\mu\nu}(x; t)$ is the field strength of the flow field B_μ and $D_\mu = \partial_\mu + [B_\mu, \cdot]$. The initial condition is $B_\mu(x; t = 0) = A_\mu(x)$, where A_μ is the original continuum gauge field. In the lattice formulation the (unsmeared) lattice link variable U replaces the continuum flow field, which we then evolve using either the tree-level improved Lüscher-Weisz pure gauge action (LW) [40] or the Wilson plaquette gauge action (W). In the continuum limit these should yield identical results, providing a check of the reliability of the limit.

The coupling at scale $\mu = 1/\sqrt{8t}$ [41] is defined via energy measurement as

$$g_{\text{GF}}^2(\mu) = \mathcal{N}^{-1} t^2 \langle E(t + \tau_0 a^2) \rangle|_{x_0=L/2, t=1/8\mu^2}, \quad (3)$$

where a is the lattice spacing. The shift parameter τ_0 is introduced to reduce the $\mathcal{O}(a^2)$ discretization effects caused by the flow [42] and can be numerically estimated during the analysis. The normalization factor \mathcal{N} for the chosen boundary conditions has been calculated in [43] to match the $\overline{\text{MS}}$ coupling in the tree level. As the translation symmetry is broken by the chosen boundary conditions, the coupling g_{GF}^2 is measured only on the central time slice $x_0 = L/2$. To quantify the effects of different discretizations, we measure the energy density $E(t)$ using both symmetric clover and simple plaquette discretizations of the flow.

In order to limit the scale into a regime where both lattice artifacts and finite volume effects are minimized, we relate the lattice and the renormalization scales by defining a dimensionless parameter c_t such that $\mu^{-1} = c_t L = \sqrt{8t}$ as described in [43, 44]. The chosen boundary conditions have a reasonably small cutoff effects and statistical variance within the range of $c_t = 0.3 - 0.5$ [43]. Value of this parameter defines the renormalization scheme.

III. EVOLUTION OF THE COUPLING

Our “benchmark” set of results presented here are obtained with gradient flow Eq. (2) evolved with Lüscher-Weisz action (LW), clover definition of energy density Eq. (3) and $c_t = 0.3$. In order to estimate systematic errors, we vary discretizations of the flow and the observable and the parameter values of the flow. The raw data is available in tables V to XII.

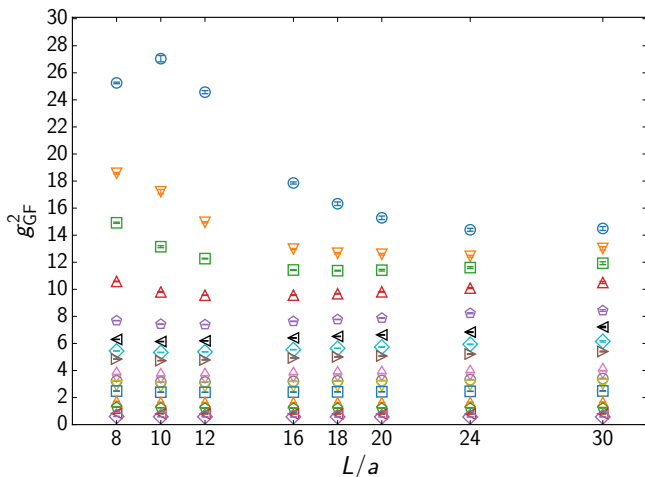


FIG. 1. The gradient flow coupling Eq. (3) measured at each β_L and L/a using the benchmark set of parameters (LW flow action, clover definition of field strength, $c_t = 0.3$).

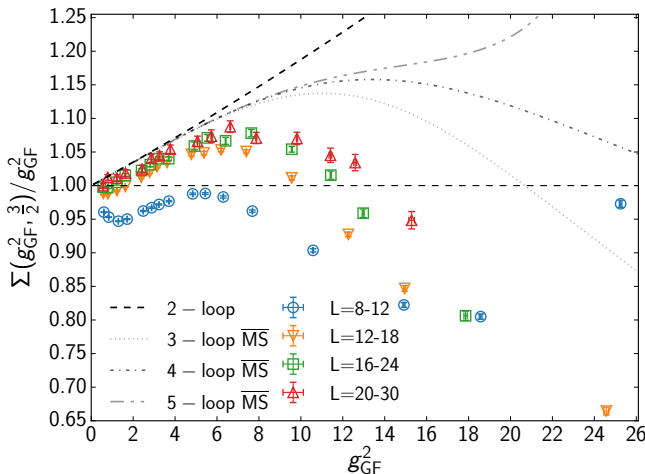


FIG. 2. The lattice step scaling function Eq. (4) obtained from the data in Fig. 1.

The measured couplings with the aforementioned parameters are shown in the top panel of Fig. 1. It is clear from the figure that the finite volume effects become substantial on smaller lattices as the coupling grows larger.

To quantify the running of the coupling we use the finite volume step scaling function [45]:

$$\Sigma(u, L/a, s) = g_{\text{GF}}^2(g_0, sL/a) \Big|_{g_{\text{GF}}^2(g_0, L/a)=u}, \quad (4)$$

which describes the change of the measured coupling when the linear size of the system is increased from L to sL . The step scaling obtained from the data in Fig. 1 is shown in Fig. 2, using a scaling factor $s = 3/2$, that is pairs of lattices with $L/a = 8 - 12$, $12 - 18$, $16 - 24$ and

c_t	L=8a	L=12a	L=16a	L=18a	L=20a	L=24a	L=30a
0.3	1.3	0.5	1.0	1.1	0.9	1.5	1.5
0.35	12	0.4	0.6	0.8	0.9	1.3	1.4
0.4	9.3	0.7	0.4	0.7	1.1	1.2	1.6
0.45	8.6	1.1	0.5	1.1	1.4	1.1	1.9

TABLE I. $\chi^2/\text{d.o.f}$ of the fit (6) at different L/a and c_t .

$20 - 30$. At the smallest volume pair $L/a = 8 - 12$ the step scaling deviates significantly from the others, and will be excluded from the continuum analysis. Rest of the volume pairs are observed to follow the scheme independent 2-loop curve in the weak coupling region up to $g_{\text{GF}}^2 \sim 6$ after which the the measured step scaling function deviates towards an IRFP around $g_{\text{GF}}^2 \sim 14$. While the higher loop $\overline{\text{MS}}$ results are scheme dependent and cannot be directly compared with our result, we show them for comparison.

For the continuum limit $\sigma(g_{\text{GF}}^2)$ of the step scaling function we use the extrapolating function

$$\Sigma(g_{\text{GF}}^2, L/a) = \sigma(g_{\text{GF}}^2) + c(g_{\text{GF}}^2)(a/L)^2. \quad (5)$$

At weak coupling the cutoff effects are regulated by the proximity of the ultraviolet fixed point, and the lowest order discretization effects of the Wilson-clover action are expected to be of order $\mathcal{O}(a^2)$, motivating the use of Eq. (5).

As will be seen below, at small couplings the $\mathcal{O}(a^2/L^2)$ extrapolation works quite well. However, at large couplings the range of volumes available to us and the accuracy of measurements are not sufficient to verify this. Using staggered fermions and much larger volumes, it has been observed that in $\text{SU}(3)$ theory with $N_f = 12$ fundamental fermions including $\mathcal{O}(a^4/L^4)$ effects can affect the continuum limit at a few 10% level [46].

At large coupling, so long as the coupling remains below the possible IRFP, the continuum limit is ultimately reached at the UV fixed point. However, due to the smallness of the β -function this would require astronomically large scale hierarchy between the lattice size L and lattice spacing a and hence is impossible to observe in simulations. Nevertheless, if the anomalous exponents of the fields remain small near the infrared fixed point, one can assume that the power counting of operators is applicable and the cutoff effects (dominated by dimension 6 operators) decrease with a power of the lattice spacing a . The naive a^2 behaviour may be modified by anomalous exponents, though. In section V we observe that the mass anomalous dimension at the IRFP remains relatively small, $\gamma_m \approx 0.28$, suggesting that the a^2 behaviour in Eq. (5) may also receive only minor corrections. The available range in our data does not allow us to numerically determine differences from Eq. (5) and hence we use it at all couplings. Near the IRFP we indeed observe that the continuum limit becomes somewhat less robust,

which is taken into account in our systematic error estimation.

In order to determine the continuum limit of the step scaling function we need the measurements of the step scaling at constant value of the coupling. However, in practice the simulations are carried out at a fixed set of bare lattice couplings which do not correspond to same value of g_{GF}^2 when a/L is varied. Hence, we adopt the customary interpolation procedure of the measured couplings to intermediate couplings. We do this using a polynomial fit¹

$$g_{\text{GF}}^2(g_0, a/L) = g_0^2 \left(1 + \sum_{i=1}^m a_i g_0^{2i} \right), \quad (6)$$

where we use $m = 10$ for lattices smaller than $L = 16$ and $m = 9$ for the larger lattices. With this choice we obtain the $\chi^2/\text{d.o.f.}$'s reported in Table I for each used c_t and in Table XVI for each used discretization. We study the robustness of the fits by repeating the analysis with m decreased by one. While this choice increases the $\chi^2/\text{d.o.f.}$, the results stay compatible with those obtained with larger m .

In Fig. 3 we show the continuum limit extrapolation of the step scaling function when g_{GF}^2 is varied from weak to strong coupling, obtained using Luscher-Weisz or Wilson flow actions and clover or plaquette field strength observables. At small couplings the continuum limit is very well under control: different discretizations extrapolate very close to the same value. At couplings $g_{\text{GF}}^2 \gtrsim 10$ the continuum limits start to show a few per cent scatter. This is taken into account in the systematic uncertainties of the final results.

The τ_0 -correction parameter in Eq. (3) can be tuned to reduce most of the $O(a^2)$ errors from the continuum limit extrapolation of the step scaling function Eq. (5). The parameter τ_0 should have a small effect in the continuum extrapolation, so long as it is not too large [47]. In practice, we have observed that τ_0 which depends logarithmically on g_{GF}^2 works well at small coupling [24]. With $c_t = 0.3$, Luscher-Weisz flow action and clover field strength observable we use

$$\tau_0 = 0.025 \log(1 + 2g_{\text{GF}}^2), \quad (7)$$

which makes the interpolation errors almost vanish at $g_{\text{GF}}^2 \lesssim 10$, as can be observed in Fig. 3. At larger couplings τ_0 correction cannot remove $O(a^2)$ significantly without ruining the continuum limit. We note that in order to have consistent $O(a^2)$ shift in the step scaling analysis, the τ_0 correction should be a function of g_{GF}^2

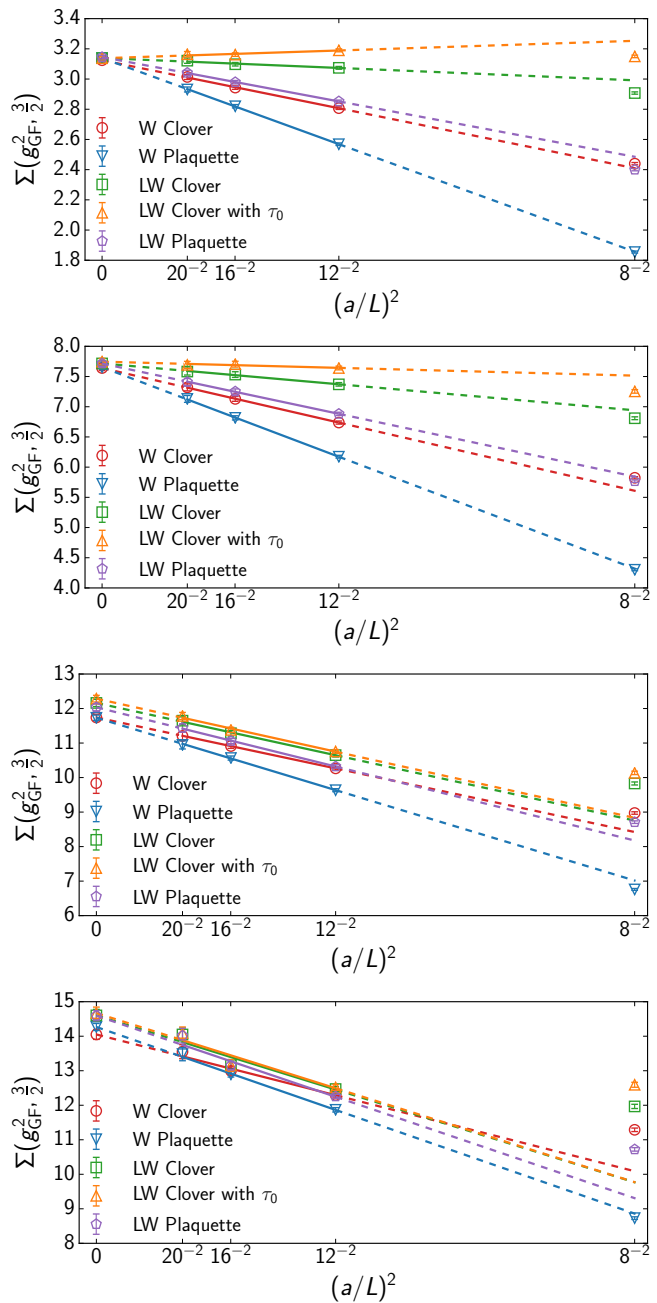


FIG. 3. The effects of the choice of the Wilson (W) and the Lüscher-Weisz (LW) flow actions, the Clover and the Plaquette field strength observables and the τ_0 correction Eq. (7) on the continuum limit of the step scaling function Eq. (5) for $c_t = 0.3$, measured at couplings (from top to bottom) $g_{\text{GF}}^2 = 3$, $g_{\text{GF}}^2 = 7$, $g_{\text{GF}}^2 = 11$ and $g_{\text{GF}}^2 = 14.5$.

instead of the bare coupling g_0^2 [30]. Because adjusting τ_0 changes the value of the measured g_{GF}^2 , the final value of τ_0 is found by iterating equations (3) and (7), starting from the initial value $g_{\text{GF}}^2 = g_0^2$.

In Fig. 4 we show the continuum limit of the step scaling at $c_t = 0.35, 0.4$ and 0.45 , evaluated at the IRFP of each c_t . The couplings $g_{\text{GF}}^2 = g_*^2$ at the fixed point are

¹ A rational interpolating function is another choice used in the literature [21, 24]. However, in our case this did not offer any improvement.

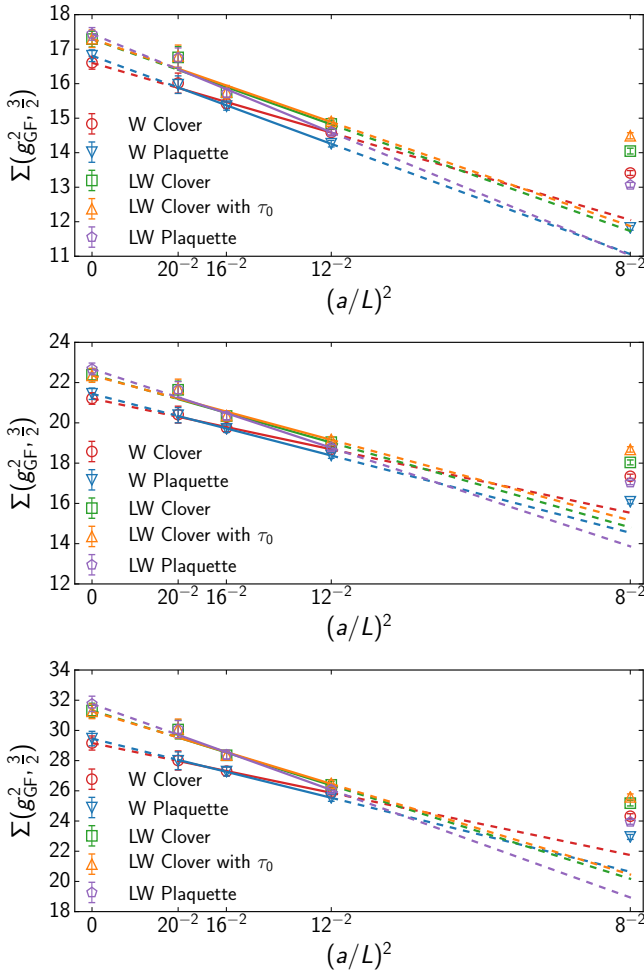


FIG. 4. *From top to bottom:* Same as Fig 3 but with: $c_t = 0.35$, $c_t = 0.4$ and $c_t = 0.45$ measured at their respective IRFP's given in Table II

shown in Table II. Because different c_t -values correspond to different coupling constant scheme, the values of g_*^2 vary significantly. It is evident that as c_t is increased the difference between the Lüscher-Weisz and Wilson flow actions grows, contributing to increasing systematic errors.

Finally, in Fig 5 we show the continuum limit of the step scaling across the full range of g_{GF}^2 at $c_t = 0.3, 0.35$ and 0.4 . The scheme independent 2-loop result and the scheme dependent 3- and 4-loop \overline{MS} results are shown as references, while the 5-loop curve from Fig. 2 is not shown here as it would mostly be outside the figure. The error bands include the statistical errors and systematic uncertainty arising from different interpolating polynomials, Eq. (6). It is evident that as c_t increases the reliability of the continuum limit extrapolation decreases, and already at $c_t = 0.4$ the final result has clearly unphysical strong “wavy” structure. This is caused by the use of the polynomial interpolation functions in Eq (6). We

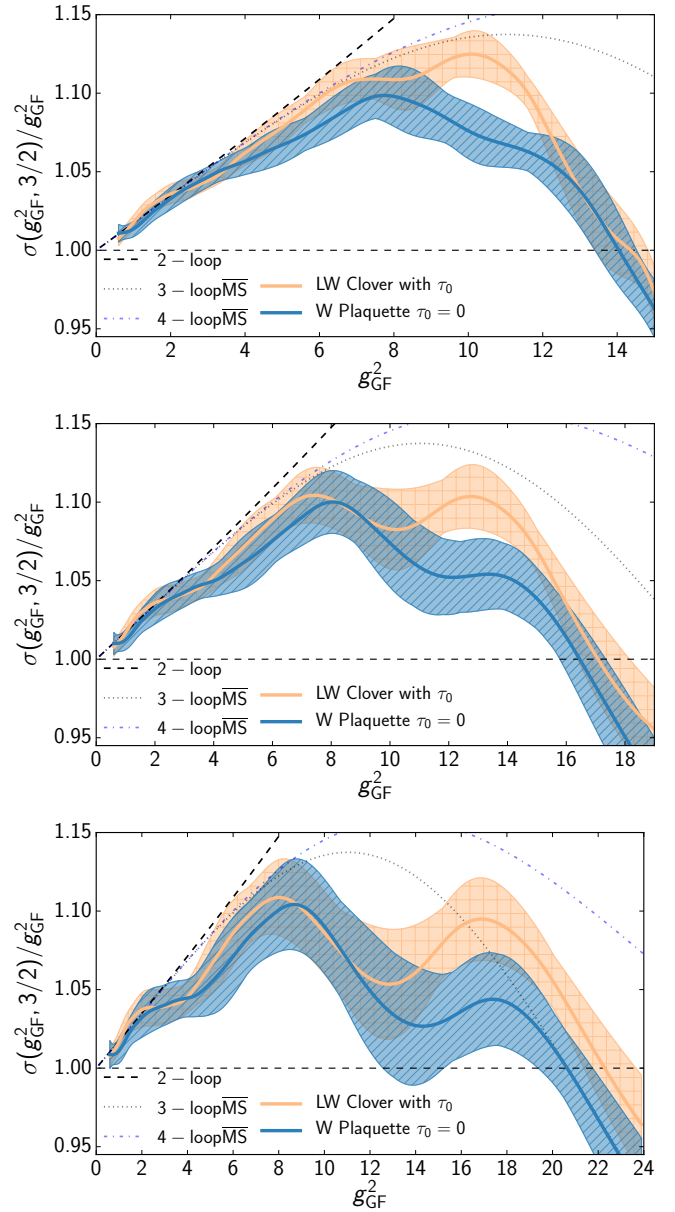


FIG. 5. *From top to bottom:* The continuum limit of the interpolated step scaling function at $c_t = 0.3, c_t = 0.35$ and $c_t = 0.4$, using discretizations which give the smallest and largest result for the step scaling function.

note that if we would use polynomials of smaller degree (for example, $m = 8$ in (6)) the wavy structure would be strongly reduced and error bands would be much narrower; however, the $\chi^2/\text{d.o.f.}$ -values would not be acceptable.

Each value of c_t corresponds to different coupling constant scheme, and the value of the fixed point coupling strongly depends on the value of c_t . The location of fixed point for each c_t is reported in Table II and individually for all discretizations of the flow in Table XIV in the appendix. The first error is the statistical uncertainty

	$c_t = 0.3$	0.35	0.4	0.45
g_*^2	14.5(4) $^{+0.4}_{-1.2}$	17.1(5) $^{+0.8}_{-1.3}$	22.2(6) $^{+1.3}_{-2.5}$	31(1) $^{+2}_{-18}$
γ_g^*	0.648(97) $^{+0.16}_{-0.1}$	0.71(12) $^{+0.17}_{-0.11}$	0.73(10) $^{+0.11}_{-0.18}$	0.75(12) $^{+0.12}_{-0.61}$

TABLE II. Measured couplings and critical exponents with different choices of parameter c_t . The error shown in parenthesis is the statistical uncertainty, and the super- and subscripts are the systematic errors due to different discretizations of the gradient flow and the field strength observables.

and the second error estimates systematic effects by including the full range of different discretization choices that were present in the Fig. 3. For our benchmark value $c_t = 0.3$ we find that our continuum extrapolated results are compatible within 1σ level with respect to all these effects except in the interval $g_{\text{GF}}^2 \in [8, 12]$ where LW and W evolved flows disagree slightly. In this case the fixed point coupling has the value $g_*^2 = 14.5(4) $^{+0.4}_{-1.2}$$

IV. LEADING IRRELEVANT CRITICAL EXPONENT

We can also obtain the leading irrelevant exponent γ_g^* at the fixed point, defined by the slope of the β -function at the IRFP. This quantity is scheme independent, and thus should not depend on c_t .

In the proximity of the fixed point we can approximate the β -function as

$$\begin{aligned} \beta(g) &= -\mu \frac{dg^2}{d\mu} \approx \gamma_g^*(g^2 - g_*^2) \\ &\approx \bar{\beta}(g) \equiv \frac{g}{2 \ln(s)} \left(1 - \frac{\sigma(g^2, s)}{g^2} \right). \end{aligned} \quad (8)$$

Measuring the slope of the step scaling function $\sigma(g^2)$ around the fixed point gives the exponent $\gamma_g^* = 0.648(97) $^{+0.16}_{-0.1}$$ at $c_t = 0.3$; the results with other c_t are shown in Table II. While there is noticeable variance between different discretizations, as indicated by the second set of errors, the result is compatible with the recent scheme independent estimate of $\gamma_g^* = 0.6515$ in Refs. [48, 49]. The results obtained with different discretizations are shown individually in Table XV. When c_t is varied, the value of γ_g^* remains constant within errors, in accord with the scheme independence of this quantity.

The results obtained above rely on the accurate continuum limit of the step scaling function $\sigma(g^2)$. However, as discussed in section III, the continuum limit may be in effect somewhat different at the close proximity of the IRFP. We can verify the consistency of the results by using a finite size scaling method developed in [50–53] to get an alternative measurement of γ_g^* . In the close proximity of the IRFP, by integrating (8) we obtain a finite size scaling relation between lattices of size L_{ref} and

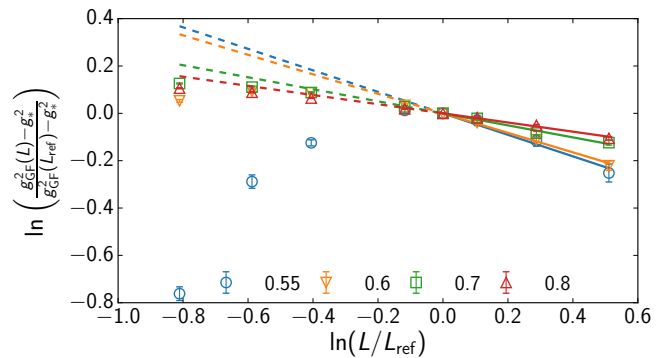


FIG. 6. Fit to function (9) for measured couplings $g_{\text{GF}}^2(\beta_L, L)$ at $\beta_L = 0.55 \dots 0.8$ at $c_t = 0.3$, using $L_{\text{ref}}/a = 18$.

L [52]:

$$g_{\text{GF}}^2(\beta_L, L) - g_*^2 = [g_{\text{GF}}^2(\beta_L, L_{\text{ref}}) - g_*^2] \left(\frac{L_{\text{ref}}}{L} \right)^{\gamma_g^*} \quad (9)$$

This equation relies on the evolution of the coupling towards the fixed point as the lattice size is increased from L_{ref} to L . Hence, it cannot be used exactly at the fixed point where there is no evolution, but only in some environment around it. We note that this also assumes vanishing discretization artifacts, and thus it can be used only if the lattices are already close enough to the continuum (L large).

In Fig. 6 we show the fit to Eq. (9) to individual measurements of g_{GF}^2 at $\beta_L \leq 0.8$, corresponding to measurements which are close to the fixed point. A good fit to Eq. (9) is obtained if we choose $L_{\text{ref}}/a \geq 18$, allowing us to extract an estimate for γ_g^* .

Instead of using individual measurements we use the interpolated values of $g_{\text{GF}}^2(\beta_L, L)$, because this allows us to freely tune the value of β_L . In Fig 7 we show the resulting γ_g^* from fits to Eq. (9), plotted as functions of $g_{\text{ref}}^2 \equiv g_{\text{GF}}^2(\beta_L, L_{\text{ref}})$. The red lines correspond to the values given in Table XV, measured from the slope of the step scaling function. The shaded error bands correspond to statistical errors while keeping the values of g_*^2 fixed to central values in Table XIV, and the dashed lines show the variation of the result if we allow g_*^2 to vary within the statistical error range.

The resulting γ_g^* is expected to be close to the true γ_g^* only in close proximity of the IRFP. However, too close to the IRFP Eq. (9) becomes unstable, which is indicated by a sudden drop in the γ_g^* measurements. Indeed, at $g_{\text{ref}}^2 \approx 12$ we observe the $c_t = 0.3$ case to give γ_g^* which is in agreement with the one obtained from the slope of the β -function. At small g_{ref}^2 the measurement of γ_g^* using Eq. 9 approaches zero.

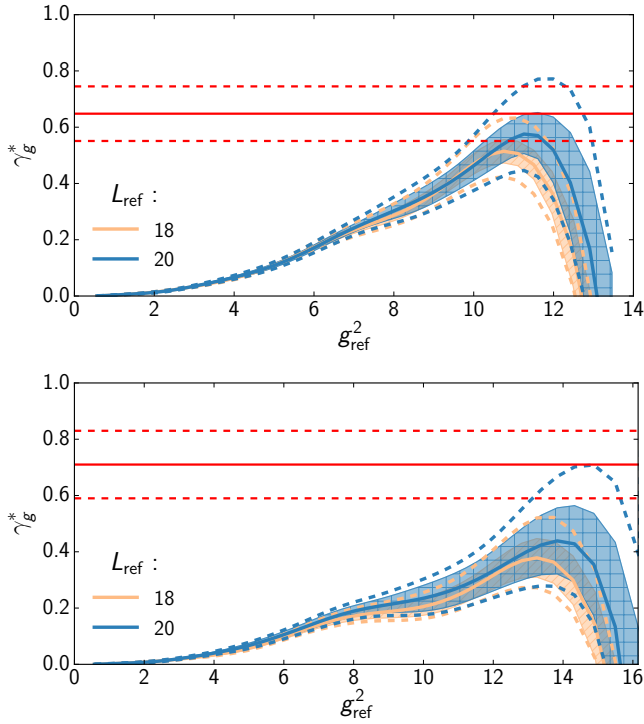


FIG. 7. Fit to function (9) for all couplings $g_{\text{GF}}^2(\beta_L, L_{\text{ref}})$ with chosen set of discretizations: *Top*: at $c_t = 0.3$, and *Bottom*: at $c_t = 0.35$. The shaded bands indicate the statistical errors for g_*^2 being the measured value, and dashed lines indicate how the result changes when g_*^2 is varied within its statistical errors.

V. ANOMALOUS DIMENSION OF THE MASS OPERATOR

In order to measure the anomalous dimension of the fermion mass operator γ_m^* we use two different methods, the mass step scaling method and the spectral density method. In the step scaling method we measure γ_m from the running of the pseudoscalar density renormalization constant [31, 54]

$$Z_P(g_0, L) = \frac{\sqrt{2f_1}}{f_P(L/2)}, \quad (10)$$

where f_P and f_1 are pseudoscalar current densities defined explicitly in e.g. [24, 38]. The mass step scaling function is defined as [31]:

$$\Sigma_P(u, s, L/a) = \left. \frac{Z_P(g_0, sL/a)}{Z_P(g_0, L/a)} \right|_{g_{\text{GF}}^2(g_0, L/a)=u} \quad (11)$$

As in the case of the coupling, we choose $s = 3/2$. The continuum limit $\sigma_P(u, s)$ is obtained by interpolating the measured Z_p by 8th order polynomials and assuming

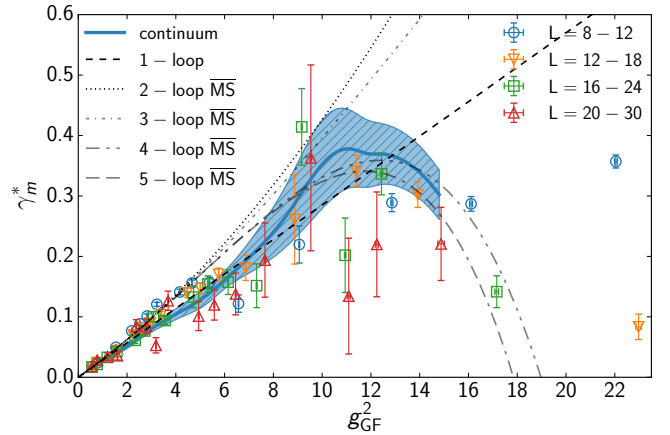


FIG. 8. The mass anomalous dimension as a function of the gradient flow coupling constant obtained using the mass step scaling function and its continuum limit. The results become unstable at large couplings.

$\mathcal{O}(a^2)$ errors. The mass anomalous dimension is then obtained as [54]

$$\gamma_m^*(u) = -\frac{\log \sigma_P(u, s)}{\log s}. \quad (12)$$

The results are shown in Fig. 8 and the raw data is given in Table XIII. The method gives results comparable to one loop perturbation theory predictions at small gauge coupling g_{GF}^2 . While the higher loop $\overline{\text{MS}}$ expansions [55, 56] are scheme dependent and cannot be directly compared to our results, it is nevertheless comforting to observe comparable behaviour between our result to the 4 and 5-loop behavior. However, the method becomes unstable at large coupling, which implies that at the fixed point $g_*^2 \approx 14.5$ the continuum limit cannot be trusted.

The second way to measure γ_m is based on the fact that it also determines the scaling of the spectral density of the massless Dirac operator. The explicit calculation of the eigenvalue distribution is prohibitively costly, but the stochastic methods [57] have made it possible to determine the mass anomalous dimension from the scaling of the mode number of the Dirac operator [32]. The mode number is known to follow a scaling behavior

$$\nu(\Lambda) \propto \Lambda^{4/(1+\gamma_m^*)}, \quad (13)$$

in some energy range between the infrared and the ultraviolet in the vicinity of a fixed point. Here γ_m^* is the mass anomalous dimension γ_m at the fixed point.

We calculate the mode number per unit volume of Eq. (13) by using

$$\nu(\Lambda) = \lim_{V \rightarrow \infty} \frac{1}{V} \langle \text{tr } \mathbb{P}(\Lambda) \rangle, \quad (14)$$

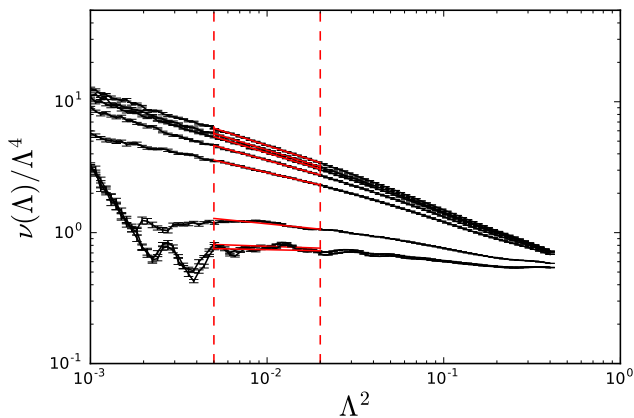


FIG. 9. The mode number divided by $a^4\Lambda^4$ as a function of $a^2\Lambda^2$ on a $L/a = 24$ lattice. The dashed red lines indicate the chosen fit range and the red solid lines the fit function. The fit ranges were varied around these chosen regions. The curves are in a descending gauge coupling order.

where the operator $\mathbb{P}(\Lambda)$ projects from the full eigenspace of $M = m^2 - \mathbb{D}^2$ to the eigenspace of eigenvalues smaller than Λ^2 . The trace is evaluated stochastically [57], and fitted to the power law behavior of Eq. (13). However, the energy range where this power law behavior holds is not known beforehand, and needs to be determined by observing the quality of the fit in a given range.

We use $L/a = 24$ lattices from the step scaling analysis, and take 12 to 20 well separated configurations for each value of the gauge coupling. We calculate the mode number for 90 values of Λ^2 ranging from 10^{-3} to 0.3. The results are then fitted to Eq. (13). The fit range is determined by varying its lower and the upper limits and observing the stability and the quality of the fit. As a cross reference at weak coupling, the fitted value of γ_m^* and the value obtained with the step scaling method are compared.

In Fig. 9 we plot the mode number divided by the fourth power of the eigenvalue scale, where the the fit range and the fit function of Eq. (13) are shown overlaid in red. According to Eq. (13) in the proximity of the fixed point the infrared behavior should be a power law in the absence of lattice artifacts. We observe this at strongest couplings, however, at small couplings the low eigenvalues appear in discrete energies, which manifests as the bumps in the mode number curve, making the power law less evident. To illustrate the evolution of the mass anomalous dimension we use the same fit range for both weak and strong couplings.

The final result of the spectral density method is shown in Fig 10, where the mass anomalous dimension γ_m^* , obtained by fitting the data with Eq. (13), is shown as a

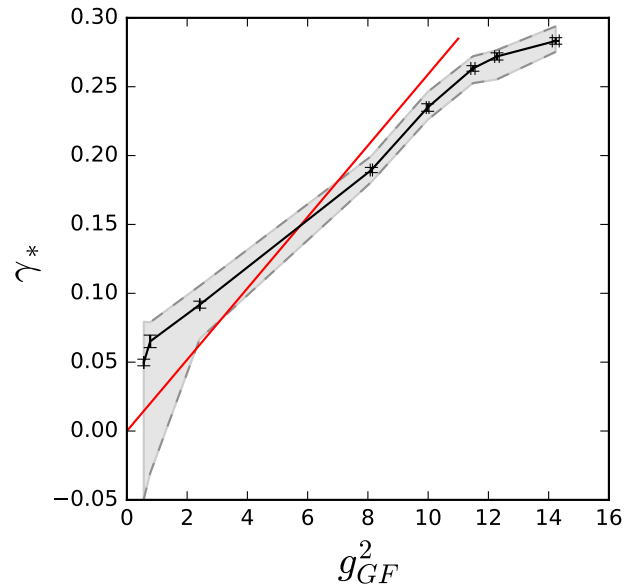


FIG. 10. The value of γ_m^* obtained by fitting Eq. (13) to the data in Fig. 9 is shown with black points and the one loop perturbative result with a red line. The shaded regions are estimates for reasonable ranges of values obtainable using the method, and were obtained by varying the fit range shown in Fig. 9 slightly.

function of the gauge coupling g_{GF}^2 . The shaded band illustrates the uncertainty resulting from varying the upper and lower limits of the fit range by $\sim 50\%$. The largest uncertainty arises at small gauge couplings, where the bumps in the data cause the changes in the fit range to change the fit dramatically. The error band of Fig. 10 becomes narrower towards the larger couplings as the ensembles near the IRFP are less sensitive to variations of the fit range.

At the fixed point $g_*^2 = 14.5$ we obtain $\gamma_m^* = 0.283(2)_{-0.01}^{+0.01}$. However, this result is obtained at fixed lattice size $L/a = 24$. A proper continuum limit requires extrapolation to infinite L , but at smaller L/a the finite size effects make the usable range for the power law fit too narrow.

Interestingly, the mass step scaling method and the spectral density method complement each other: while the mass step scaling is stable and accurate at weak couplings, where the spectral density method fails, at strong coupling the roles are reversed.

VI. CONCLUSIONS

We have studied the running coupling in the SU(2) lattice gauge theory with 6 fermions in the fundamental representation. Gradient flow algorithm with Dirichlet boundaries was shown to provide robust results on the

large coupling behavior of this theory giving a result consistent with the existence of IRFP at $g_*^2 = 14.5(4)_{-1.2}^{+0.4}$ in our benchmark scheme. The scheme-independent slope of β -function at IRFP was measured to be $\gamma_g^* = 0.648(97)_{-0.1}^{+0.16}$.

We also determined the mass anomalous dimension γ_m in this theory using the spectral density method and the mass step scaling method. The step scaling method gives results compatible with perturbation theory at weak coupling. At intermediate couplings the step scaling method can be matched on the results from the spectral density method which remain stable in the vicinity of the fixed point where the step scaling computation breaks down. With the spectral density method we estimated the mass anomalous dimension at the fixed point as $\gamma_m^* = 0.283(2)_{-0.01}^{+0.01}$, albeit a proper continuum limit is still lacking.

Our results are consistent with the existence of a strong

coupling IRFP and indicate that the SU(2) gauge theory with six fermion flavors in the fundamental representation is within the conformal window. The theory likely is near the lower boundary of the conformal window, which makes it an interesting candidate for beyond the standard model theories: when coupled with the electroweak gauge currents the chiral symmetries are explicitly broken, the theory is pulled outside the conformal window and may constitute a concrete example of a walking technicolor theory.

ACKNOWLEDGMENTS

This work is supported by the Academy of Finland grants 267286 and 267842. V.L and J.M.S. are supported by the Jenny and Antti Wihuri foundation and S.T. by the Magnus Ehrnrooth foundation. The simulations were performed at the Finnish IT Center for Science (CSC), Espoo, Finland.

-
- [1] C. Pica, *Proceedings, 34th International Symposium on Lattice Field Theory (Lattice 2016): Southampton, UK, July 24-30, 2016*, PoS, **LATTICE2016**, 015 (2016), [arXiv:1701.07782 \[hep-lat\]](#).
- [2] D. Negradi and A. Patella, *Int. J. Mod. Phys.*, **A31**, 1643003 (2016), [arXiv:1607.07638 \[hep-lat\]](#).
- [3] T. DeGrand, *Rev. Mod. Phys.*, **88**, 015001 (2016), [arXiv:1510.05018 \[hep-ph\]](#).
- [4] A. J. Hietanen, J. Rantaharju, K. Rummukainen, and K. Tuominen, *JHEP*, **05**, 025 (2009), [arXiv:0812.1467 \[hep-lat\]](#).
- [5] A. J. Hietanen, K. Rummukainen, and K. Tuominen, *Phys. Rev.*, **D80**, 094504 (2009), [arXiv:0904.0864 \[hep-lat\]](#).
- [6] L. Del Debbio, A. Patella, and C. Pica, *Phys. Rev.*, **D81**, 094503 (2010), [arXiv:0805.2058 \[hep-lat\]](#).
- [7] S. Catterall, J. Giedt, F. Sannino, and J. Schneible, *JHEP*, **11**, 009 (2008), [arXiv:0807.0792 \[hep-lat\]](#).
- [8] F. Bursa, L. Del Debbio, L. Keegan, C. Pica, and T. Pickup, *Phys. Rev.*, **D81**, 014505 (2010), [arXiv:0910.4535 \[hep-ph\]](#).
- [9] L. Del Debbio, B. Lucini, A. Patella, C. Pica, and A. Rago, *Phys. Rev.*, **D80**, 074507 (2009), [arXiv:0907.3896 \[hep-lat\]](#).
- [10] L. Del Debbio, B. Lucini, A. Patella, C. Pica, and A. Rago, *Phys. Rev.*, **D82**, 014510 (2010), [arXiv:1004.3206 \[hep-lat\]](#).
- [11] L. Del Debbio, B. Lucini, A. Patella, C. Pica, and A. Rago, *Phys. Rev.*, **D82**, 014509 (2010), [arXiv:1004.3197 \[hep-lat\]](#).
- [12] F. Bursa, L. Del Debbio, D. Henty, E. Kerrane, B. Lucini, A. Patella, C. Pica, T. Pickup, and A. Rago, *Phys. Rev.*, **D84**, 034506 (2011), [arXiv:1104.4301 \[hep-lat\]](#).
- [13] T. DeGrand, Y. Shamir, and B. Svetitsky, *Phys. Rev.*, **D83**, 074507 (2011), [arXiv:1102.2843 \[hep-lat\]](#).
- [14] A. Patella, *Phys. Rev.*, **D86**, 025006 (2012), [arXiv:1204.4432 \[hep-lat\]](#).
- [15] J. Giedt and E. Weinberg, *Phys. Rev.*, **D85**, 097503 (2012), [arXiv:1201.6262 \[hep-lat\]](#).
- [16] L. Del Debbio, B. Lucini, A. Patella, C. Pica, and A. Rago, *Phys. Rev.*, **D93**, 054505 (2016), [arXiv:1512.08242 \[hep-lat\]](#).
- [17] J. Rantaharju, T. Rantalaiho, K. Rummukainen, and K. Tuominen, *Phys. Rev.*, **D93**, 094509 (2016), [arXiv:1510.03335 \[hep-lat\]](#).
- [18] J. Rantaharju, *Phys. Rev.*, **D93**, 094516 (2016), [arXiv:1512.02793 \[hep-lat\]](#).
- [19] H. Ohki, T. Aoyama, E. Itou, M. Kurachi, C. J. D. Lin, H. Matsufuru, T. Onogi, E. Shintani, and T. Yamazaki, *Proceedings, 28th International Symposium on Lattice field theory (Lattice 2010)*, PoS, **LATTICE2010**, 066 (2010), [arXiv:1011.0373 \[hep-lat\]](#).
- [20] F. Bursa, L. Del Debbio, L. Keegan, C. Pica, and T. Pickup, *Phys. Lett.*, **B696**, 374 (2011), [arXiv:1007.3067 \[hep-ph\]](#).
- [21] T. Karavirta, J. Rantaharju, K. Rummukainen, and K. Tuominen, *JHEP*, **05**, 003 (2012), [arXiv:1111.4104 \[hep-lat\]](#).
- [22] M. Hayakawa, K. I. Ishikawa, S. Takeda, M. Tomii, and N. Yamada, *Phys. Rev.*, **D88**, 094506 (2013), [arXiv:1307.6696 \[hep-lat\]](#).
- [23] T. Appelquist, R. Brower, M. Buchoff, M. Cheng, G. Fleming, J. Kiskis, M. Lin, E. Neil, J. Osborn, C. Rebbi, *et al.*, *Phys. Rev. Lett.*, **112**, 111601 (2014), [arXiv:1311.4889 \[hep-ph\]](#).
- [24] V. Leino, J. Rantaharju, T. Rantalaiho, K. Rummukainen, J. M. Suorsa, and K. Tuominen, *Phys. Rev. D*, **95**, 114516 (2017), [arXiv:1701.04666 \[hep-lat\]](#).
- [25] T. Banks and A. Zaks, *Nucl. Phys.*, **B196**, 189 (1982).
- [26] F. Herzog, B. Ruijl, T. Ueda, J. A. M. Vermaseren, and A. Vogt, *JHEP*, **02**, 090 (2017), [arXiv:1701.01404 \[hep-ph\]](#).

- [27] Z. Fodor, K. Holland, J. Kuti, S. Mondal, D. Nogradi, and C. H. Wong, Phys. Rev., **D94**, 091501 (2016), [arXiv:1607.06121 \[hep-lat\]](#).
- [28] R. Narayanan and H. Neuberger, JHEP, **03**, 064 (2006), [arXiv:hep-th/0601210 \[hep-th\]](#).
- [29] M. Luscher, Commun. Math. Phys., **293**, 899 (2010), [arXiv:0907.5491 \[hep-lat\]](#).
- [30] A. Ramos, *Proceedings, 32nd International Symposium on Lattice Field Theory (Lattice 2014): Brookhaven, NY, USA, June 23-28, 2014*, PoS, **LATTICE2014**, 017 (2015), [arXiv:1506.00118 \[hep-lat\]](#).
- [31] S. Capitani, M. Luscher, R. Sommer, and H. Wittig (ALPHA), Nucl. Phys., **B544**, 669 (1999), [arXiv:hep-lat/9810063 \[hep-lat\]](#).
- [32] A. Patella, Phys. Rev., **D84**, 125033 (2011), [arXiv:1106.3494 \[hep-th\]](#).
- [33] S. Capitani, S. Durr, and C. Hoelbling, JHEP, **11**, 028 (2006), [arXiv:hep-lat/0607006 \[hep-lat\]](#).
- [34] T. DeGrand, Y. Shamir, and B. Svetitsky, *Proceedings, 29th International Symposium on Lattice field theory (Lattice 2011): Squaw Valley, Lake Tahoe, USA, July 10-16, 2011*, PoS, **LATTICE2011**, 060 (2011), [arXiv:1110.6845 \[hep-lat\]](#).
- [35] I. P. Omelyan, I. M. Mryglod, and R. Folk, Computer Physics Communications, **151**, 272 (2003).
- [36] T. Takaishi and P. de Forcrand, Phys. Rev., **E73**, 036706 (2006), [arXiv:hep-lat/0505020 \[hep-lat\]](#).
- [37] R. C. Brower, T. Ivanenko, A. R. Levi, and K. N. Orginos, Nucl. Phys., **B484**, 353 (1997), [arXiv:hep-lat/9509012 \[hep-lat\]](#).
- [38] M. Luscher and P. Weisz, Nucl. Phys., **B479**, 429 (1996), [arXiv:hep-lat/9606016 \[hep-lat\]](#).
- [39] M. Luscher and P. Weisz, JHEP, **02**, 051 (2011), [arXiv:1101.0963 \[hep-th\]](#).
- [40] M. Luscher and P. Weisz, Commun. Math. Phys., **97**, 59 (1985), [Erratum: Commun. Math. Phys.98,433(1985)].
- [41] M. Luscher, JHEP, **08**, 071 (2010), [Erratum: JHEP03,092(2014)], [arXiv:1006.4518 \[hep-lat\]](#).
- [42] A. Cheng, A. Hasenfratz, Y. Liu, G. Petropoulos, and D. Schaich, JHEP, **05**, 137 (2014), [arXiv:1404.0984 \[hep-lat\]](#).
- [43] P. Fritzsche and A. Ramos, JHEP, **10**, 008 (2013), [arXiv:1301.4388 \[hep-lat\]](#).
- [44] Z. Fodor, K. Holland, J. Kuti, D. Nogradi, and C. H. Wong, JHEP, **11**, 007 (2012), [arXiv:1208.1051 \[hep-lat\]](#).
- [45] M. Luscher, R. Sommer, P. Weisz, and U. Wolff, Nucl. Phys., **B413**, 481 (1994), [arXiv:hep-lat/9309005 \[hep-lat\]](#).
- [46] Z. Fodor, K. Holland, J. Kuti, D. Nogradi, and C. H. Wong, Phys. Lett., **B779**, 230 (2018), [arXiv:1710.09262 \[hep-lat\]](#).
- [47] A. Hasenfratz, D. Schaich, and A. Veernala, JHEP, **06**, 143 (2015), [arXiv:1410.5886 \[hep-lat\]](#).
- [48] T. A. Ryttov and R. Shrock, Phys. Rev., **D95**, 105004 (2017), [arXiv:1703.08558 \[hep-th\]](#).
- [49] T. A. Ryttov and R. Shrock, Phys. Rev., **D95**, 085012 (2017), [arXiv:1701.06083 \[hep-th\]](#).
- [50] T. Appelquist, G. T. Fleming, and E. T. Neil, Phys. Rev., **D79**, 076010 (2009), [arXiv:0901.3766 \[hep-ph\]](#).
- [51] T. DeGrand and A. Hasenfratz, Phys. Rev., **D80**, 034506 (2009), [arXiv:0906.1976 \[hep-lat\]](#).
- [52] C. J. D. Lin, K. Ogawa, and A. Ramos, JHEP, **12**, 103 (2015), [arXiv:1510.05755 \[hep-lat\]](#).
- [53] A. Hasenfratz and D. Schaich, JHEP, **02**, 132 (2018), [arXiv:1610.10004 \[hep-lat\]](#).
- [54] M. Della Morte, R. Hoffmann, F. Knechtli, J. Rolf, R. Sommer, I. Wetzorke, and U. Wolff (ALPHA), Nucl. Phys., **B729**, 117 (2005), [arXiv:hep-lat/0507035 \[hep-lat\]](#).
- [55] J. A. M. Vermaseren, S. A. Larin, and T. van Ritbergen, Phys. Lett., **B405**, 327 (1997), [arXiv:hep-ph/9703284 \[hep-ph\]](#).
- [56] T. Luthe, A. Maier, P. Marquard, and Y. Schröder, JHEP, **01**, 081 (2017), [arXiv:1612.05512 \[hep-ph\]](#).
- [57] L. Giusti and M. Luscher, JHEP, **03**, 013 (2009), [arXiv:0812.3638 \[hep-lat\]](#).

TABLE III. The measured $\kappa_c(\beta_L)$ at $L/a = 24$ for each β_L .

β_L	κ_c	β_L	κ_c	β_L	κ_c	β_L	κ_c
8	0.125310366353981	2	0.127533813721664	1	0.131448889150607	0.6	0.136438136224601
6	0.125459579958083	1.7	0.128194200995596	0.9	0.132331360707040	0.55	0.137424583321490
4	0.125860459184944	1.5	0.128799165934744	0.8	0.133419041876613	0.53	0.137839481272905
3	0.126367585261215	1.3	0.129603737388233	0.7	0.134765027707880	0.5	0.138504981089103

Appendix A: Tables

TABLE IV. Number of trajectories for each β_L and L after thermalization.

β_L	$N(L = 8)$	$N(L = 10)$	$N(L = 12)$	$N(L = 16)$	$N(L = 18)$	$N(L = 20)$	$N(L = 24)$	$N(L = 30)$
8	81351	10849	78537	8500	6468	11473	62574	7383
6	157185	20468	89006	122197	95460	40434	33845	6098
4	95516	20604	84883	106793	86888	41198	14031	5963
3	101614	23139	88269	102191	82956	39127	21475	8520
2	94905	17527	82783	94976	76712	35925	40449	9146
1.7	93581	19990	79821	92194	74062	34220	36175	8785
1.5	92038	19268	113427	90364	70024	32955	21173	10895
1.3	89055	18380	110383	88057	69042	31553	32209	12014
1	85016	16659	105548	75659	75037	33030	19082	11730
0.9	100759	22780	106021	77452	72799	46582	47578	15254
0.8	78037	29807	135876	95623	97127	71468	42482	21425
0.7	130058	30235	134124	90815	105578	43926	20925	20403
0.6	126248	30284	121780	146073	93686	68932	62787	19478
0.55	131577	22127	123599	103778	88999	42183	28736	16607
0.53	137302	24401	146940	84434	43674	64683	29323	15825
0.5	128873	23648	99971	86445	26464	39693	23994	15355

TABLE V. The measured gradient flow couplings g_{GF}^2 with the chosen set of parameters: LW evolved flow, clover definition of energy density, $c_t = 0.3$ and $\tau_0 = 0.025 \log(1 + 2 * g_{GF}^2)$. These are the parameters used in most of the work. The statistical errors are counted with the jackknife method.

β_L	$L = 8$	$L = 10$	$L = 12$	$L = 16$	$L = 18$	$L = 20$	$L = 24$	$L = 30$
8	0.56878(16)	0.5639(5)	0.56447(17)	0.5642(8)	0.5660(14)	0.5660(9)	0.5674(5)	0.5687(19)
6	0.77786(18)	0.7718(5)	0.7718(3)	0.7754(4)	0.7760(5)	0.7776(6)	0.7808(10)	0.792(3)
4	1.1816(3)	1.1736(11)	1.1781(5)	1.1913(6)	1.1960(9)	1.2012(15)	1.212(2)	1.224(5)
3	1.5426(6)	1.5383(14)	1.5546(9)	1.5827(12)	1.5933(16)	1.607(2)	1.630(4)	1.653(7)
2	2.1936(10)	2.213(3)	2.2591(18)	2.329(2)	2.357(2)	2.379(4)	2.423(5)	2.466(12)
1.7	2.5286(15)	2.559(3)	2.6261(19)	2.726(2)	2.765(4)	2.803(6)	2.863(7)	2.951(16)
1.5	2.8258(14)	2.881(4)	2.956(2)	3.083(3)	3.142(3)	3.184(8)	3.268(9)	3.368(17)
1.3	3.2215(19)	3.295(5)	3.396(3)	3.563(4)	3.638(6)	3.684(9)	3.781(9)	3.93(2)
1	4.163(3)	4.283(6)	4.460(4)	4.730(6)	4.846(9)	4.939(14)	5.11(2)	5.33(3)
0.9	4.665(3)	4.822(9)	5.008(5)	5.317(8)	5.456(12)	5.577(15)	5.82(2)	6.07(4)
0.8	5.383(7)	5.538(14)	5.755(5)	6.145(16)	6.302(14)	6.451(18)	6.70(2)	7.12(5)
0.7	6.570(8)	6.69(2)	6.867(10)	7.314(19)	7.509(15)	7.65(2)	8.06(3)	8.32(6)
0.6	9.06(2)	8.83(3)	8.876(14)	9.16(2)	9.34(2)	9.53(2)	9.88(3)	10.36(7)
0.55	12.86(4)	11.86(7)	11.39(2)	10.94(2)	10.98(2)	11.09(6)	11.37(6)	11.77(10)
0.53	16.10(6)	15.59(16)	13.92(5)	12.43(4)	12.24(5)	12.24(6)	12.19(7)	12.85(12)
0.5	22.04(5)	24.6(2)	22.97(11)	17.16(7)	15.80(12)	14.87(13)	14.12(10)	14.30(14)

TABLE VI. The measured gradient flow couplings g_{GF}^2 with otherwise same parameters as **V** but with $\tau_0 = 0$.

β_L	$L = 8$	$L = 10$	$L = 12$	$L = 16$	$L = 18$	$L = 20$	$L = 24$	$L = 30$
8	0.60287(17)	0.5851(5)	0.57911(17)	0.5724(8)	0.5724(14)	0.5712(9)	0.5710(5)	0.5711(19)
6	0.83581(19)	0.8078(6)	0.7966(3)	0.7893(4)	0.7869(5)	0.7865(6)	0.7870(10)	0.796(3)
4	1.2955(3)	1.2443(12)	1.2268(5)	1.2189(6)	1.2178(9)	1.2190(15)	1.225(2)	1.232(6)
3	1.7145(6)	1.6456(15)	1.6290(10)	1.6252(12)	1.6271(16)	1.635(2)	1.650(4)	1.665(7)
2	2.4813(11)	2.396(3)	2.3875(18)	2.404(2)	2.417(2)	2.428(4)	2.458(5)	2.488(12)
1.7	2.8793(16)	2.782(3)	2.784(2)	2.819(2)	2.840(4)	2.864(6)	2.907(7)	2.980(16)
1.5	3.2339(15)	3.143(4)	3.143(2)	3.193(3)	3.231(3)	3.257(8)	3.321(9)	3.403(17)
1.3	3.707(2)	3.610(5)	3.621(3)	3.696(4)	3.746(7)	3.773(9)	3.845(9)	3.97(2)
1	4.839(3)	4.725(7)	4.780(4)	4.923(6)	5.002(9)	5.069(14)	5.21(2)	5.40(3)
0.9	5.441(3)	5.332(10)	5.377(5)	5.540(8)	5.638(12)	5.729(15)	5.93(2)	6.15(4)
0.8	6.297(7)	6.139(15)	6.191(6)	6.410(16)	6.518(14)	6.632(18)	6.83(2)	7.21(5)
0.7	7.687(9)	7.42(2)	7.396(10)	7.635(19)	7.772(15)	7.87(2)	8.23(4)	8.43(6)
0.6	10.58(2)	9.80(3)	9.562(15)	9.56(2)	9.67(2)	9.81(2)	10.08(3)	10.50(7)
0.55	14.91(4)	13.14(7)	12.26(2)	11.42(2)	11.37(2)	11.41(6)	11.60(6)	11.92(10)
0.53	18.57(6)	17.21(16)	14.95(5)	12.97(4)	12.66(5)	12.59(6)	12.44(7)	13.02(12)
0.5	25.25(6)	27.0(2)	24.57(11)	17.85(7)	16.32(13)	15.28(13)	14.39(10)	14.49(14)

TABLE VII. The measured gradient flow couplings g_{GF}^2 with otherwise same parameters as VI but with $c_t = 0.35$.

β_L	$L = 8$	$L = 10$	$L = 12$	$L = 16$	$L = 18$	$L = 20$	$L = 24$	$L = 30$
8	0.5911(2)	0.5808(6)	0.5771(2)	0.5727(10)	0.5739(19)	0.5734(12)	0.5739(6)	0.574(2)
6	0.8194(2)	0.8030(7)	0.7957(4)	0.7930(5)	0.7917(7)	0.7918(8)	0.7933(13)	0.804(4)
4	1.2754(5)	1.2453(16)	1.2341(8)	1.2330(8)	1.2336(13)	1.236(2)	1.245(3)	1.249(7)
3	1.7015(8)	1.659(2)	1.6533(14)	1.6575(16)	1.661(2)	1.672(3)	1.690(5)	1.711(10)
2	2.5077(16)	2.459(4)	2.462(2)	2.491(3)	2.507(3)	2.518(6)	2.549(8)	2.583(16)
1.7	2.939(2)	2.881(5)	2.897(2)	2.945(3)	2.969(6)	3.000(10)	3.045(10)	3.12(2)
1.5	3.330(2)	3.284(6)	3.294(3)	3.359(5)	3.404(5)	3.436(13)	3.502(13)	3.59(2)
1.3	3.863(3)	3.809(8)	3.833(5)	3.926(7)	3.985(11)	4.008(13)	4.083(14)	4.23(3)
1	5.174(6)	5.101(11)	5.186(7)	5.351(10)	5.451(15)	5.51(2)	5.68(4)	5.90(5)
0.9	5.906(6)	5.855(17)	5.903(10)	6.090(14)	6.21(2)	6.30(2)	6.54(3)	6.80(8)
0.8	7.005(14)	6.87(2)	6.928(11)	7.18(3)	7.30(2)	7.42(3)	7.64(5)	8.15(9)
0.7	8.946(17)	8.64(4)	8.55(2)	8.83(3)	8.96(3)	9.05(4)	9.47(7)	9.62(10)
0.6	13.12(3)	12.06(5)	11.66(2)	11.54(3)	11.62(4)	11.76(4)	12.02(6)	12.48(12)
0.55	19.72(7)	17.03(12)	15.68(4)	14.25(4)	14.09(5)	14.05(10)	14.23(11)	14.52(18)
0.53	25.51(10)	23.4(2)	19.89(8)	16.67(7)	16.11(9)	15.90(11)	15.50(12)	16.1(2)
0.5	36.17(9)	38.9(3)	35.18(18)	24.61(13)	22.0(2)	20.2(2)	18.66(18)	18.5(2)

TABLE VIII. The measured gradient flow couplings g_{GF}^2 with otherwise same parameters as VI but with $c_t = 0.4$.

β_L	$L = 8$	$L = 10$	$L = 12$	$L = 16$	$L = 18$	$L = 20$	$L = 24$	$L = 30$
8	0.5851(2)	0.5793(8)	0.5774(3)	0.5745(13)	0.576(2)	0.5770(16)	0.5779(8)	0.578(3)
6	0.8132(2)	0.8035(9)	0.7992(5)	0.7999(6)	0.7993(8)	0.7998(10)	0.8020(17)	0.814(5)
4	1.2769(6)	1.258(2)	1.2511(10)	1.2546(10)	1.2563(18)	1.260(2)	1.272(5)	1.271(9)
3	1.7227(11)	1.693(2)	1.6944(18)	1.703(2)	1.708(2)	1.721(4)	1.742(7)	1.770(13)
2	2.597(2)	2.564(6)	2.572(3)	2.609(4)	2.627(5)	2.638(9)	2.670(12)	2.70(2)
1.7	3.082(3)	3.037(7)	3.058(4)	3.115(5)	3.142(8)	3.180(14)	3.227(15)	3.30(3)
1.5	3.531(3)	3.498(10)	3.509(4)	3.583(8)	3.638(8)	3.676(18)	3.743(19)	3.84(3)
1.3	4.156(5)	4.107(12)	4.133(7)	4.241(10)	4.312(17)	4.327(19)	4.40(2)	4.59(4)
1	5.760(10)	5.66(2)	5.779(12)	5.959(15)	6.09(2)	6.13(3)	6.35(6)	6.60(8)
0.9	6.709(11)	6.66(3)	6.686(18)	6.89(2)	7.04(4)	7.12(4)	7.42(6)	7.74(13)
0.8	8.24(2)	8.03(5)	8.06(2)	8.35(6)	8.48(5)	8.62(6)	8.87(9)	9.60(18)
0.7	11.21(3)	10.70(8)	10.46(4)	10.80(7)	10.89(6)	10.95(8)	11.40(13)	11.46(18)
0.6	17.58(6)	15.98(9)	15.29(4)	14.94(6)	14.96(7)	15.07(8)	15.29(10)	15.7(2)
0.55	27.66(12)	23.5(2)	21.42(8)	18.99(8)	18.66(9)	18.48(18)	18.64(18)	18.8(3)
0.53	36.70(17)	33.6(4)	28.14(14)	22.90(13)	21.90(17)	21.4(2)	20.6(2)	21.3(3)
0.5	53.35(15)	57.8(5)	52.5(3)	35.9(2)	31.7(3)	28.7(4)	25.8(3)	25.3(4)

TABLE IX. The measured gradient flow couplings g_{GF}^2 with otherwise same parameters as VI but with $c_t = 0.45$.

β_L	$L = 8$	$L = 10$	$L = 12$	$L = 16$	$L = 18$	$L = 20$	$L = 24$	$L = 30$
8	0.5832(2)	0.5800(10)	0.5794(3)	0.5775(16)	0.580(3)	0.581(2)	0.5831(10)	0.583(3)
6	0.8142(3)	0.8079(11)	0.8060(6)	0.8095(8)	0.8094(11)	0.8100(13)	0.813(2)	0.825(7)
4	1.2935(8)	1.280(2)	1.2761(13)	1.2827(14)	1.285(2)	1.290(3)	1.307(6)	1.299(11)
3	1.7686(15)	1.744(3)	1.750(2)	1.761(2)	1.768(3)	1.782(5)	1.807(9)	1.843(17)
2	2.737(3)	2.706(9)	2.718(4)	2.762(5)	2.780(7)	2.792(13)	2.822(17)	2.86(2)
1.7	3.297(4)	3.249(10)	3.272(5)	3.335(7)	3.364(11)	3.41(2)	3.45(2)	3.53(4)
1.5	3.828(6)	3.788(14)	3.793(6)	3.874(12)	3.939(12)	3.98(2)	4.05(2)	4.17(4)
1.3	4.587(8)	4.513(19)	4.533(9)	4.657(15)	4.74(2)	4.74(2)	4.82(3)	5.05(6)
1	6.644(19)	6.48(3)	6.61(2)	6.80(2)	6.99(4)	7.00(6)	7.29(10)	7.59(14)
0.9	7.95(2)	7.87(5)	7.82(3)	8.04(4)	8.25(9)	8.30(7)	8.70(12)	9.1(2)
0.8	10.27(6)	9.85(11)	9.80(4)	10.14(11)	10.30(10)	10.43(12)	10.72(17)	11.8(3)
0.7	15.28(7)	14.20(17)	13.68(8)	14.10(15)	14.09(13)	14.07(18)	14.5(2)	14.4(3)
0.6	25.73(10)	23.15(15)	21.96(8)	21.14(10)	21.04(12)	21.07(14)	21.17(16)	21.6(3)
0.55	41.4(2)	34.9(3)	31.59(14)	27.40(14)	26.75(16)	26.3(3)	26.4(3)	26.4(5)
0.53	55.6(2)	51.1(7)	42.5(2)	33.8(2)	32.0(3)	31.2(3)	29.6(3)	30.3(6)
0.5	81.7(2)	89.6(9)	82.0(4)	55.5(3)	48.5(6)	43.4(7)	38.4(5)	37.1(7)

TABLE X. The measured gradient flow couplings g_{GF}^2 with otherwise same parameters as VI but with wilson flow (W).

β_L	$L = 8$	$L = 10$	$L = 12$	$L = 16$	$L = 18$	$L = 20$	$L = 24$	$L = 30$
8	0.7777(2)	0.6961(5)	0.65497(18)	0.6141(8)	0.6053(14)	0.5977(9)	0.5894(5)	0.5828(19)
6	1.0912(2)	0.9682(6)	0.9055(3)	0.8492(4)	0.8340(5)	0.8245(6)	0.8135(10)	0.813(3)
4	1.7257(4)	1.5102(13)	1.4069(6)	1.3182(6)	1.2960(9)	1.2823(15)	1.269(2)	1.261(6)
3	2.3150(7)	2.0152(16)	1.8797(10)	1.7643(12)	1.7370(16)	1.724(2)	1.712(4)	1.706(7)
2	3.4037(13)	2.966(3)	2.7779(19)	2.623(2)	2.591(2)	2.570(4)	2.558(6)	2.554(12)
1.7	3.9705(19)	3.458(3)	3.250(2)	3.083(2)	3.050(4)	3.036(7)	3.029(7)	3.061(16)
1.5	4.4776(17)	3.919(4)	3.677(2)	3.497(3)	3.474(4)	3.456(9)	3.463(9)	3.497(17)
1.3	5.155(2)	4.517(6)	4.249(3)	4.056(5)	4.034(7)	4.009(9)	4.014(9)	4.09(2)
1	6.778(4)	5.953(7)	5.634(4)	5.418(6)	5.401(9)	5.398(14)	5.45(2)	5.56(3)
0.9	7.633(4)	6.724(11)	6.350(5)	6.105(8)	6.094(13)	6.106(15)	6.20(2)	6.33(4)
0.8	8.827(8)	7.752(15)	7.318(6)	7.068(16)	7.050(14)	7.072(19)	7.15(2)	7.42(5)
0.7	10.691(9)	9.34(2)	8.735(10)	8.413(19)	8.401(15)	8.39(2)	8.60(4)	8.66(6)
0.6	14.40(2)	12.24(3)	11.227(16)	10.50(2)	10.42(2)	10.42(2)	10.48(3)	10.69(7)
0.55	19.60(5)	16.15(8)	14.24(3)	12.46(2)	12.18(2)	12.03(6)	11.98(6)	12.01(10)
0.53	23.82(7)	20.77(18)	17.17(5)	14.05(4)	13.48(5)	13.20(6)	12.77(7)	12.97(12)
0.5	31.43(6)	31.9(2)	27.60(12)	19.01(7)	17.10(13)	15.82(13)	14.61(10)	14.25(13)

TABLE XI. The measured gradient flow couplings g_{GF}^2 with otherwise same parameters as VI but with Plaquette measurement of energy density.

β_L	$L = 8$	$L = 10$	$L = 12$	$L = 16$	$L = 18$	$L = 20$	$L = 24$	$L = 30$
8	0.8059(2)	0.6984(6)	0.6528(2)	0.6117(8)	0.6030(15)	0.5955(9)	0.5878(5)	0.581(2)
6	1.1209(2)	0.9649(6)	0.8986(3)	0.8434(4)	0.8289(5)	0.8204(6)	0.8102(10)	0.810(3)
4	1.7448(4)	1.4880(14)	1.3845(6)	1.3027(6)	1.2833(9)	1.2714(15)	1.260(2)	1.255(6)
3	2.3125(7)	1.9679(17)	1.8379(10)	1.7368(12)	1.7149(16)	1.705(2)	1.699(4)	1.696(7)
2	3.3486(13)	2.865(3)	2.6927(19)	2.569(2)	2.546(2)	2.533(4)	2.531(6)	2.534(12)
1.7	3.885(2)	3.328(3)	3.140(2)	3.012(2)	2.992(4)	2.988(7)	2.994(7)	3.037(16)
1.5	4.365(2)	3.758(5)	3.545(2)	3.412(3)	3.403(4)	3.397(9)	3.420(9)	3.468(17)
1.3	5.008(2)	4.316(6)	4.084(3)	3.949(5)	3.947(7)	3.935(9)	3.959(9)	4.05(2)
1	6.549(4)	5.653(7)	5.392(4)	5.262(6)	5.272(9)	5.287(14)	5.36(2)	5.50(3)
0.9	7.376(4)	6.378(11)	6.066(6)	5.921(9)	5.943(13)	5.977(15)	6.11(2)	6.26(5)
0.8	8.555(9)	7.348(16)	6.986(6)	6.851(16)	6.868(14)	6.918(19)	7.04(3)	7.35(5)
0.7	10.492(11)	8.89(2)	8.351(10)	8.16(2)	8.192(15)	8.22(2)	8.48(4)	8.59(6)
0.6	14.78(3)	11.85(4)	10.850(16)	10.25(2)	10.21(2)	10.25(2)	10.41(3)	10.73(8)
0.55	21.61(7)	16.18(9)	14.04(3)	12.29(3)	12.04(3)	11.95(6)	12.00(6)	12.22(10)
0.53	27.60(10)	21.5(2)	17.26(6)	14.00(4)	13.43(5)	13.22(7)	12.89(7)	13.37(13)
0.5	39.08(10)	35.2(3)	29.15(14)	19.43(8)	17.43(14)	16.12(13)	14.96(11)	14.91(14)

TABLE XII. The measured gradient flow couplings g_{GF}^2 with otherwise same parameters as VI but with Plaquette measurement of energy density and with wilson flow (W).

β_L	$L = 8$	$L = 10$	$L = 12$	$L = 16$	$L = 18$	$L = 20$	$L = 24$	$L = 30$
8	1.1442(2)	0.8610(6)	0.7497(2)	0.6592(8)	0.6393(15)	0.6242(9)	0.6073(5)	0.593(2)
6	1.6195(2)	1.2003(7)	1.0377(3)	0.9115(4)	0.8809(5)	0.8616(6)	0.8381(10)	0.828(3)
4	2.5970(5)	1.8793(15)	1.6142(6)	1.4154(6)	1.3696(10)	1.3400(15)	1.307(2)	1.285(6)
3	3.5106(8)	2.5118(18)	2.1574(11)	1.8946(13)	1.8363(17)	1.802(2)	1.765(4)	1.738(7)
2	5.2024(16)	3.705(4)	3.190(2)	2.818(2)	2.738(2)	2.687(4)	2.637(6)	2.602(12)
1.7	6.086(2)	4.325(4)	3.733(2)	3.311(2)	3.223(4)	3.174(7)	3.123(7)	3.120(16)
1.5	6.882(2)	4.902(5)	4.227(2)	3.757(3)	3.671(4)	3.612(9)	3.570(9)	3.565(17)
1.3	7.954(3)	5.657(6)	4.885(3)	4.357(5)	4.265(7)	4.190(9)	4.137(9)	4.16(2)
1	10.554(5)	7.476(8)	6.484(5)	5.824(7)	5.713(9)	5.644(14)	5.61(2)	5.67(3)
0.9	11.947(6)	8.454(12)	7.313(6)	6.563(9)	6.446(13)	6.386(15)	6.39(2)	6.45(5)
0.8	13.914(10)	9.771(18)	8.436(6)	7.600(17)	7.456(15)	7.396(19)	7.38(3)	7.57(5)
0.7	17.038(14)	11.82(2)	10.083(11)	9.05(2)	8.889(15)	8.78(2)	8.87(4)	8.83(6)
0.6	23.68(4)	15.69(4)	13.037(17)	11.32(2)	11.04(2)	10.91(2)	10.83(3)	10.92(8)
0.55	33.67(10)	21.21(11)	16.71(3)	13.48(3)	12.94(3)	12.62(6)	12.39(6)	12.27(10)
0.53	42.17(14)	27.9(2)	20.37(6)	15.25(4)	14.34(5)	13.87(7)	13.22(7)	13.26(12)
0.5	58.45(14)	45.2(4)	33.94(16)	20.82(9)	18.30(14)	16.70(13)	15.14(11)	14.59(14)

TABLE XIII. The measured bare values of Z_P for each lattice size L and β_L . The step scaling mass anomalous dimension is computed from these using the steps given in the main text.

β_L	$L = 8$	$L = 10$	$L = 12$	$L = 16$	$L = 18$	$L = 20$	$L = 24$	$L = 30$
8	0.97103(6)	0.9670(2)	0.96430(10)	0.9600(3)	0.9578(6)	0.9568(3)	0.9534(2)	0.9499(6)
6	0.95990(8)	0.9545(2)	0.95067(14)	0.94396(12)	0.9413(2)	0.9405(3)	0.9358(4)	0.9298(12)
4	0.991(3)	0.9279(4)	0.9646(2)	0.9130(2)	0.9097(3)	0.9055(6)	0.9009(11)	0.893(2)
3	0.9135(2)	0.9023(5)	0.8953(3)	0.8835(4)	0.8794(4)	0.8734(9)	0.8684(12)	0.860(2)
2	0.8749(3)	0.8615(9)	0.8481(5)	0.8328(6)	0.8244(8)	0.8176(13)	0.8124(16)	0.790(3)
1.7	0.8557(4)	0.8408(11)	0.8256(6)	0.8080(8)	0.7988(8)	0.7920(16)	0.7833(18)	0.765(3)
1.5	0.8407(6)	0.8204(13)	0.8068(6)	0.7859(8)	0.7780(9)	0.7696(18)	0.754(2)	0.753(3)
1.3	0.8219(8)	0.7979(16)	0.7827(7)	0.7601(7)	0.7506(12)	0.746(2)	0.7316(19)	0.708(4)
1	0.7734(8)	0.749(2)	0.7304(10)	0.7016(17)	0.6902(18)	0.677(2)	0.664(4)	0.650(6)
0.9	0.7468(10)	0.717(2)	0.7010(10)	0.6733(18)	0.660(2)	0.646(2)	0.632(2)	0.615(6)
0.8	0.703(2)	0.680(3)	0.6603(14)	0.6344(18)	0.616(2)	0.609(3)	0.595(4)	0.576(7)
0.7	0.618(2)	0.597(5)	0.588(2)	0.548(3)	0.546(3)	0.539(5)	0.515(7)	0.498(10)
0.6	0.411(2)	0.401(6)	0.376(4)	0.346(3)	0.338(9)	0.328(10)	0.293(7)	0.283(15)
0.55	0.3450(13)	0.323(4)	0.3068(16)	0.275(2)	0.267(2)	0.252(3)	0.253(5)	0.239(8)
0.53	0.3193(10)	0.299(3)	0.2842(11)	0.2619(16)	0.2514(19)	0.249(2)	0.228(2)	0.227(7)
0.5	0.2803(7)	0.254(2)	0.2425(7)	0.2356(9)	0.2345(18)	0.229(2)	0.222(2)	0.209(4)

TABLE XIV. Location of the IRFP for different discretizations: LW=Lüscher-Weisz, W=Wilson, $\tau_0 = \tau_0 - \text{correction}$, C=Clover and P=Plaquette.

c_t	$LWC\tau_0$	LWC	LCP	WC	WP
0.3	14.5(4)	14.1(3)	14.3(2)	13.5(2)	14.0(2)
0.35	17.1(5)	17.1(2)	17.5(4)	16.1(3)	16.4(3)
0.4	22.2(6)	22.3(6)	22.9(6)	20.2(5)	20.5(5)
0.45	31(1)	31.1(9)	32(1)	27(14)	26(15)

TABLE XV. Value of γ_g^* measured from slope of the β -function for different discretizations: LW=Lüscher-Weisz, W=Wilson, $\tau_0 = \tau_0 - \text{correction}$, C=Clover and P=Plaquette.

c_t	$LWC\tau_0$	LWC	LCP	WC	WP
0.3	0.648(97)	0.68(9)	0.74(10)	0.8(1)	0.77(10)
0.35	0.71(12)	0.699(85)	0.69(9)	0.76(12)	0.70(12)
0.4	0.73(10)	0.74(10)	0.74(10)	0.69(14)	0.59(16)
0.45	0.75(12)	0.75(11)	0.74(11)	0.51(39)	0.40(28)

TABLE XVI. Combined $\chi^2/\text{d.o.f}$ of the beta interpolations in use (6) at different c_t and available discretization options.

c_t	$LWC\tau_0$	LWC	LCP	WC	WP
0.3	1.29	1.32	1.57	1.56	2.51
0.35	1.09	1.11	1.21	1.19	1.51
0.4	1.12	1.12	1.17	1.16	1.29
0.45	1.43	1.41	1.45	1.41	1.47